Geophysical Journal International

Geophys. J. Int. (2013) doi: 10.1093/gji/ggt237

Geophysical Journal International Advance Access published July 18, 2013

Thermal inertia mapping and its application in mineral exploration: results from Mamandur polymetal prospect, India

D. Ramakrishnan, Rishikesh Bharti, K.D. Singh and M. Nithya

Department of Earth Sciences, Indian Institute of Technology Bombay, Mumbai-400076, India. E-mail: ramakrish@iitb.ac.in

Accepted 2013 June 17. Received 2013 June 14; in original form 2012 December 10

SUMMARY

Thermal anomalies associated with ore-mineralization (Pb–Cu–Zn and Fe) were studied using thermal infrared data collected over Mamandur polymetal prospect, India, with the aid of satellite, field, and laboratory measurements. Day and night ASTER data were analysed in conjunction with field measurements to estimate thermal inertia of the ore body, altered zones and country rocks. Representative samples collected from field were also analysed for thermal conductivity, diffusivity, and inertia using a self-fabricated setup. Spatial changes in thermal inertia were mapped by look up table (LUT) and advanced thermal inertia mapping (ATIM) approaches. Mineralized zones show very high thermal contrast (ΔT) both in field (15–25°C) and satellite data (14.9–16.9 °C). They also exhibit the lowest thermal inertia in field-(2118–5474 J m^{-2} K^{-1} s$^{-1/2}$) and satellite-based (3783–4037 J m^{-2} K^{-1} s$^{-1/2}$) measurements. In non-mineralized areas, acidic rocks (granite, migmatite and granite gneiss) have lower inertia than basic rocks (basic granulite, dolerite and charnockite). Results estimated by LUT and ATIM approaches correlate very well at satellite ($R^2 = 0.97$) and field ($R^2 = 0.89$) scales. Similarly, field- and satellite-based results also have good correlation ($R^2 = 0.69$–0.72). This study illustrates the potential of thermal inertia mapping in delineating ore bodies and deciphering the lithological changes even under veneer of soil.

Key words: Image processing; Spatial analysis; Heat flow; Heat generation & transport.

1 INTRODUCTION

Thermal inertia (TI), the resistance offered by a material to temperature change, is an important physical property that can be used to identify or discriminate among materials. This lumped property can be expressed as

$$\mathrm{TI} = \sqrt{k\rho c}, \quad (1)$$

where TI is the thermal inertia (J m^{-2} K^{-1} s$^{-1/2}$), k is the thermal conductivity (J m^{-1} s^{-1} K^{-1}), ρ is the density (kg m^{-3}) and c is the specific heat (J kg^{-1} K^{-1}). Heat transfer in materials with high thermal inertia leads to small changes in temperature, while low thermal inertia leads to large changes in temperature (Gillespie & Kahle 1977; Price 1977; Pratt & Ellyett 1979). Thermal properties of rocks and soils measured using laboratory or bore-hole logging techniques are being successfully employed in mineral investigation (Facer *et al.* 1980; Zolotarev 1989; Prensky 1992; Mwenifumbo 1993), petrophysics and hydrocarbon exploration (Beck 1976; Vasseur *et al.* 1995; Schön 2004, 2011; Nasipuri *et al.* 2006; El Sayed 2011), geotechnical engineering (Jougnot & Revil 2010) and lithological discrimination (Bosch *et al.* 2002). However, these techniques have limited utility in spatial discrimination and mapping of rocks and soils. On the other hand, thermal inertia estimated from satellite/airborne infrared sensors is more efficient in discriminating and mapping rocks and soils (Watson 1971, 1973; Kahle *et al.* 1976; Gillespie & Kahle 1977; Price 1977; Pratt & Ellyett 1979; Kahle 1987; Christensen & Malin 1988; Mellon *et al.* 2000; Mitra & Majumdar 2004; Putzig *et al.* 2004; Nasipuri *et al.* 2006; Nowicki & Christensen 2007). Remotely sensed thermal images corresponding to diurnal (heating–cooling) phases of any surface can be employed to map and monitor this parameter on a larger areal extent. Watson (1971, 1973, 1975) generated thermal inertia map using remote sensing data based on one-dimensional heat transfer theory. Subsequently, Kahle (1977) applied a finite difference technique that takes heating terms (sensible and latent) into account in the heat balance equation to compute thermal inertia. TI estimated using remotely measured infrared and visible bands has now been extensively used in various applications like soil water estimation (Lu *et al.* 2009; Minacapilli *et al.* 2009), land mine detection (Nash 1988; Van Dam *et al.* 2004; Deans *et al.* 2006), geology and planetary exploration (Kahle *et al.* 1976; Pratt & Ellyett 1979; Kahle 1987; Christensen & Malin 1988; Mellon *et al.* 2000; Mitra & Majumdar 2004; Putzig *et al.* 2004; Nasipuri *et al.* 2006; Nowicki & Christensen 2007; Putzig & Mellon 2007), urban heat island (Cai *et al.* 2008) and geothermal anomaly mapping (Eneva *et al.* 2006; Coolbaugh *et al.* 2007). However, relatively few publications address the application of remotely estimated thermal inertia in mineral exploration (Thompson & Baker 1981; Nasipuri *et al.* 2006; Gupta *et al.* 2009).

Further, TI is sensitive to composition and density of near surface materials up to a depth that can be reached by the diurnal heating wave (∼30–50 cm) (Schieldge *et al.* 1980). Hence, mapping thermal inertia of surfaces can provide additional information about compositional changes at the surface and shallow depth.

In this study, we demonstrate a method to delineate ore bodies and discriminate rock types in and around Mamandur polymetal prospect, India, using satellite, field and laboratory data. This shear zone- and metamorphism-related mineralization offers one of the best sites in the world to study the massive type Pre-Cambrian polymetal deposits. The procedure adopted herein involves (i) generation of thermal inertia maps using daytime, nighttime satellite and field data; (ii) discrimination of ore bodies and rock types based on thermal inertia; (iii) analyses of field samples in laboratory for mineralogy and thermal properties, and (iv) correlation of results for accuracy assessment.

2 STUDY AREA

The Mamandur polymetal prospect (Fig. 1) is bounded by northern latitudes 11° 52′ to 12° 01′ and eastern longitudes 78° 53′ to 78° 59′. This area is situated in the northern part of the southern granulite terrain (SGT) comprising mostly migmatite and charnockite with bands of other high-grade metamorphic rocks such as banded-magnetite–quartzite (BMQ), garnet–biotite–gneiss, granite–gneiss and garnet–biotite–sillimanite–gneiss. These rocks are cut across by dykes of norite, dolerite, granite pegmatite and quartz veins (Chattopadhyay 1999). The Pb, Cu and Zn mineralization in this area is associated with a shear separating migmatite complex in the east and amphibolite charnockite in the west. In this deposit, mineralization occurs in two distinct zones. A disseminated copper lode occurs in the southern part and a multimetal mineralization zone with lead–zinc–copper and silver values occurs in the northern part. Wall rock alteration is manifested by alteration of biotite into chlorite and sericite; feldspars into kaolinite; and pyroxene to tremolite and actinolite. Besides Pb, Cu and Zn mineralization, the investigated area is also hosting banded magnetite quartzite deposits. The mineralogy of ore bodies, alteration zones and host rocks are detailed in Section 5.1.

3 THEORY

One-dimensional heat transfer is the simplest and a reasonably well-understood concept. For low-heat conducting materials such as rocks and soils, 1-D transient heat transfer equations are widely used to estimate thermal conductivity and diffusivity (Carslaw & Jaeger 1959; Woodside & Messmer 1961; Morabito 1989; Middleton 1993; Schilling 1999; Abu-Hamdeh 2003; Bautista & Campos 2005; ASTM 2008, 2009a,b).

For terrestrial and planetary applications, the temperature gradient across the thickness of conducting media cannot be measured. Hence, TI is estimated by comparing temperature differences of surfaces collected at different phases of diurnal heating–cooling cycle to values predicted by temperature diffusion models (Kahle 1977). Under such conditions, the heat transfer equation can be expressed as

$$\frac{\partial T}{\partial t} = \frac{k}{\rho.c}.\frac{\partial^2 T}{\partial x^2}, \tag{2}$$

where k is the thermal conductivity (J m^{-1} s^{-1} K^{-1}), ρ is the density (kg m^{-3}), c is the specific heat (J kg^{-1} K^{-1}), T is the temperature

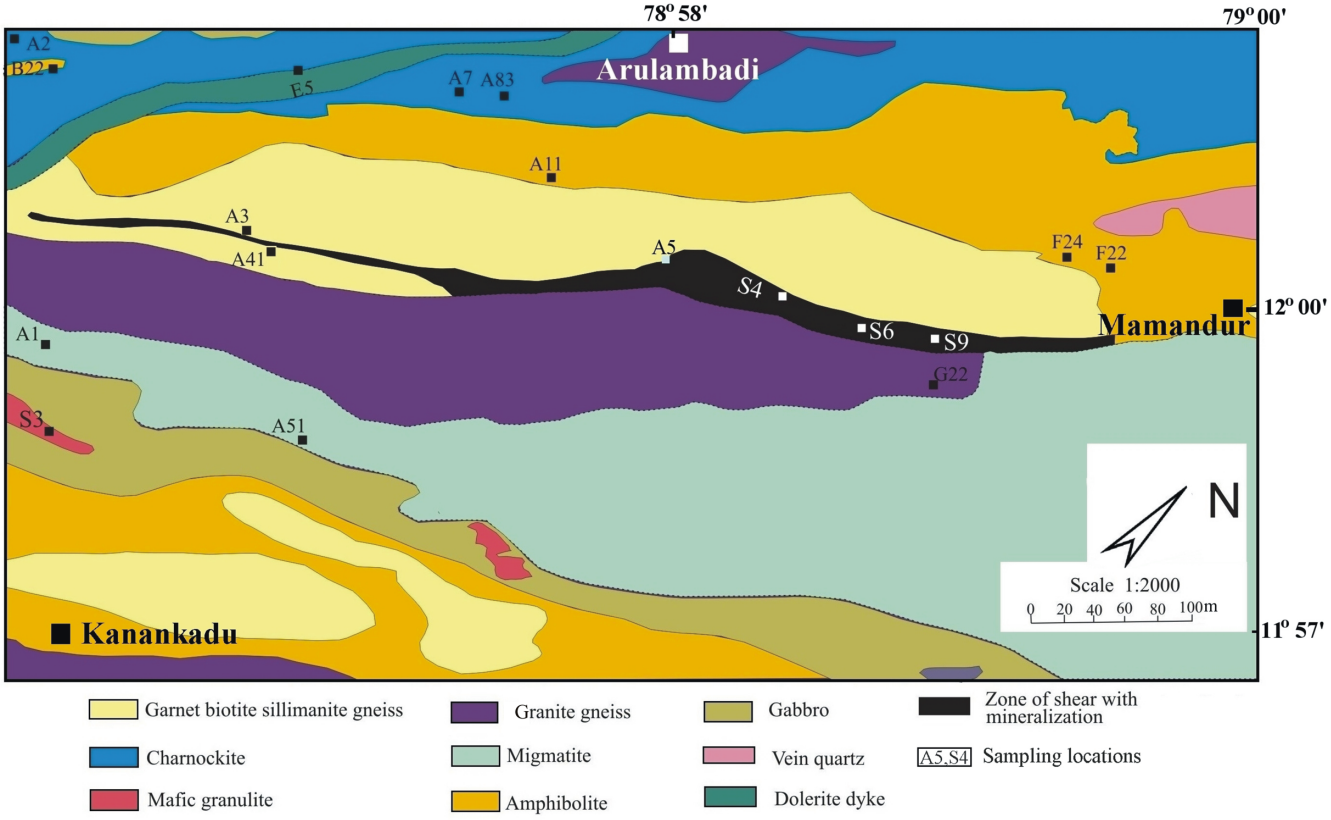

Figure 1. Geological map of the Mamandur prospect indicating the sites of field investigation and sampling.

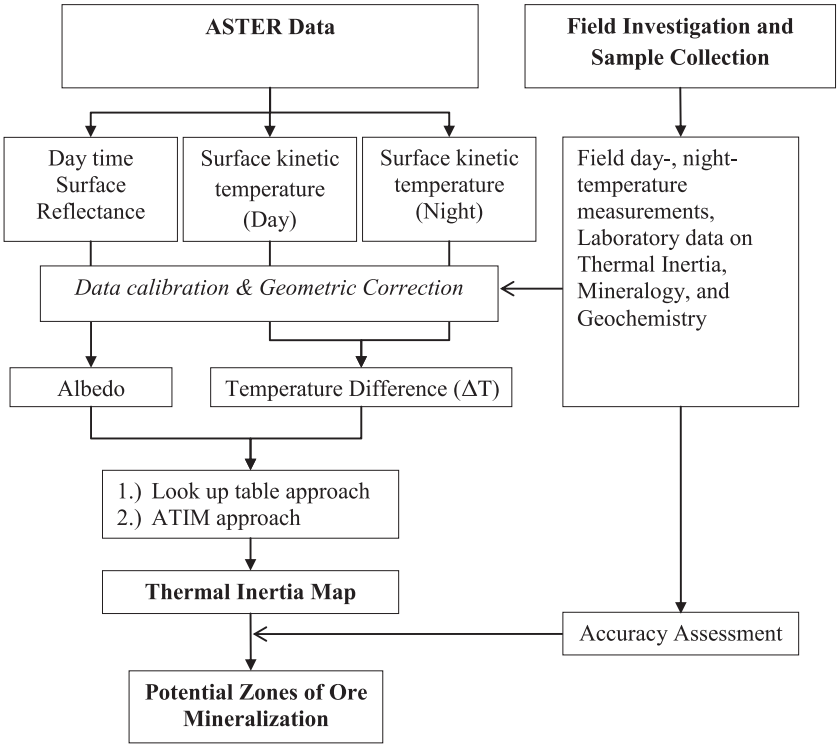

Figure 2. Flowchart depicting the methodology adopted.

(°K), t the duration of heating (h) and x the depth to diurnal temperature variations.

It is considered that beyond 1 m depth, the diurnal variations due to solar heating ceases (Kahle 1977). Hence, for all practical applications involving solar-heating-related heat transfer, a maximum depth of 1 m is considered. Xue & Cracknell (1995) have developed an advanced thermal inertia model (ATIM) by using phase angle information of the diurnal temperature change. Eq. (3) is based on first-order approximation thermal inertia model and is suitable for areas with variable soil moisture and vegetation cover having surface temperature ranging from 280 to 310 °K.

$$TI = \frac{(1-\beta)S_0C_t}{\Delta T\sqrt{\omega}}\left\{\frac{A_1[\cos(\omega t_2-\delta_1)-\cos(\omega t_1-\delta_1)]}{\sqrt{1+\frac{1}{b}+\frac{1}{2b^2}}}\right.$$
$$\left.+\frac{A_2[\cos(\omega t_2-\delta_2)-\cos(\omega t_1-\delta_2)]}{\sqrt{2+\frac{\sqrt{2}}{b}+\frac{1}{2b^2}}}\right\}, \quad (3)$$

where 'β' is albedo derived from the satellite data, S_0 is the Solar constant (W m^{-2}), C_t is the atmospheric transmittance, ω is the Earth's angular frequency, ΔT is the temperature difference (°K),

Table 1. Specifications of instruments and data used.

Instruments/data product	Application	Accuracy of measurement	Central wavelength (μm)	Spatial resolution
Fabricated instrument for thermal conductivity and diffusivity measurement	Laboratory	Conductivity ± 0.1–0.3 J m^{-1} K^{-1} s^{-1}	Not applicable	Sample size (9 cm × 9 cm × 1.5 cm)
FLUKE Ti-27 IR imager	Field cum laboratory	Thermal sensitivity ±0.05 °C	Band-1 (0.45) Band-2 (0.57) Band-3 (0.66) Band-4 (10.5)	FOV: 23°×17° IFOV : 1.67 mRad
AST-07	Field	Not applicable	Band-1 (0.56) Band-2 (0.66) Band-3 (0.82) Band-4 (1.65) Band-5 (2.17) Band-6 (2.21) Band-7 (2.27) Band-8 (2.33) Band-9 (2.39)	15 m 15 m 15 m 30 m 30 m 30 m 30 m 30 m 30 m
AST-2B03	Field	Not applicable	Band-1 (10.5)	90 m

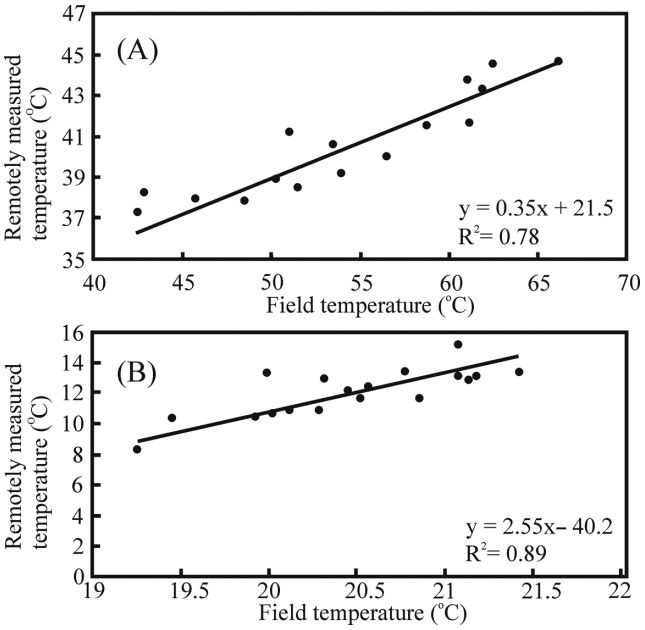

Figure 3. Scatter plot showing the correlation between satellite- and field-measured temperatures for different locations corresponding to daytime (A) and nighttime (B) measurements.

A_n is Fourier series coefficient, t_1 and t_2 are time of day and night satellite overpass and 'b' is dependent on maximum daytime temperature (Eq. 4) estimated from the nearest weather station.

$$b = \frac{\tan(\omega t_{\max})}{1 - \tan(\omega t_{\max})}, \tag{4}$$

δ_1 (Eq. 5) and δ_2 (Eq. 6) are phase differences and is a function of maximum daytime temperature. Phase difference can be calculated using the following equations:

$$\delta_1 = \arctan\left(\frac{b}{1+b}\right), \tag{5}$$

$$\delta_2 = \arctan\left(\frac{b\sqrt{2}}{1+b\sqrt{2}}\right). \tag{6}$$

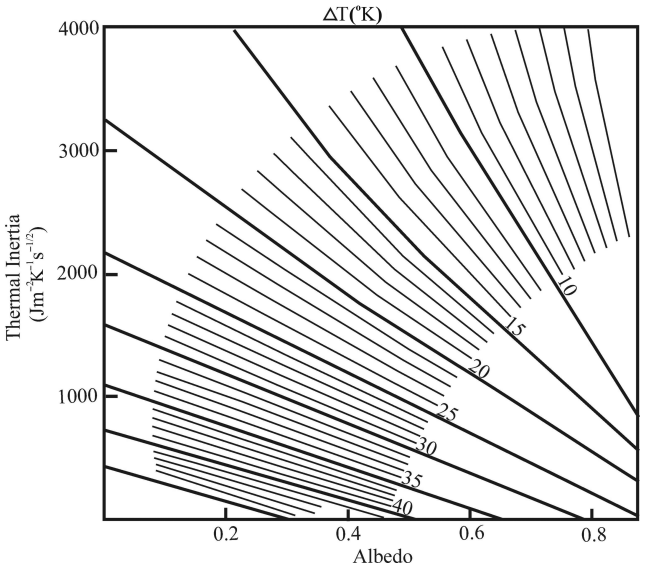

Figure 4. LUT model to relate thermal inertia (P), albedo (β) and thermal contrast (ΔT).

The Fourier series coefficient A_n (Eq. 7) can be expressed as

$$A_n = \frac{2\sin\delta\sin\vartheta}{n\pi}\sin(n\psi) + \frac{2\cos\delta\cos\vartheta}{\pi(n^2-1)}.[n\sin(n\psi)\cos\psi - \cos(n\psi)\sin\psi], \tag{7}$$

where $n = 1, 2, 3\ldots$, δ is the Solar declination, ϑ is the local latitude and ψ is a function of Solar declination and latitude (Eq. 8) and can be defined as

$$\psi = \arccos(\tan\delta\tan\vartheta). \tag{8}$$

Alternate to this procedure is the look up table (LUT) approach that relates ΔT as a function of albedo (β), slope, azimuth and thermal inertia (Kahle 1977). For a flat area without topography-related effects, variables such as slope and azimuth can be dropped and LUT relates the thermal inertia of surface to ΔT and 'β' (Pratt & Ellyett 1979). With ΔT and 'β' known for each pixel of the satellite data, TI of ground targets can be estimated using a calibration chart that can be modelled for a set of conditions and diurnal temperature variations (Price 1977; Pratt & Ellyett 1979).

4 METHODOLOGY

The adopted methodology in this study involves, 1) normalization of ASTER (albedo, daytime and nighttime surface kinetic

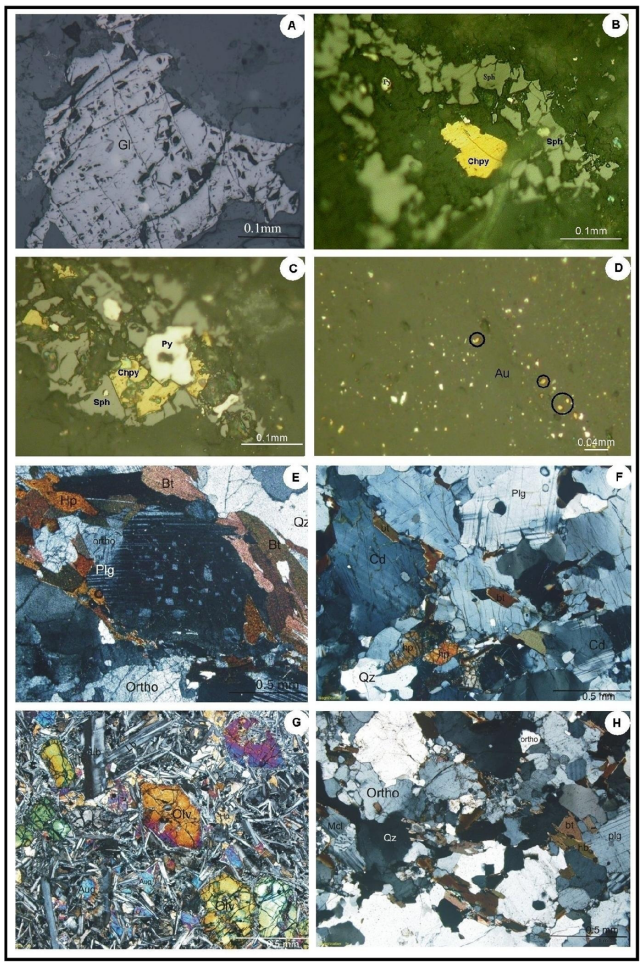

Figure 5. Photomicrographs of ore body (A–D) and host rocks (E–H) relating the compositional changes to thermal properties.

temperatures) data with field data, 2) generation of thermal inertia map by LUT and ATIM techniques, 3) estimation of field TI and collection of representative samples, 4) estimation of lab-based thermal inertia and mineralogy of ores, rocks and soils and 5) assessment of accuracy. The adopted methodology is shown as a flowchart (Fig. 2).

4.1 ASTER data pre-processing

4.1.1 Normalization of daytime and nighttime images

In this study, we have used the atmospherically corrected surface reflectance (AST07) and surface kinetic temperatures (AST2B03) data from United States Geological Survey (USGS) and Japanese Aerospace Exploration Agency (JAXA). The technological specifications of ASTER and other data products used in this study are given in Table 1. The chosen data sets correspond to the period October and February 2001 and 2005 as thermal contrast (ΔT) between day and night was maximum during these periods. As our data acquisition request (DAR) could not yield successive daytime and nighttime data, we adopted a unique procedure to transform the multiple date images to single date (day and night) measurements. This involved measurement of albedo and temperature in the field (at 27 locations with GPS coordinates) using a FLUKE Ti-27 thermal imaging camera. This camera has three visible bands and a thermal band. The daytime measurements were made between 11 a.m. and 2 p.m. and, nighttime measurements were made between 8 and 10 p.m. with Sunset around 5:30 p.m. At each site, the areal extent of measurements varied from 1.0–1.5 m^2.

The field albedo of rock and soil exposures was measured by normalizing the image radiances with spectralon panel radiance. The thermal band was calibrated with the aid of a thermoelectrically stabilized blackbody reference. The emissivity of rocks (where thermal images were acquired) was measured using the designs and prototype (D&P) 102F Fourier Transform Infrared spectrometer (FTIR) following the procedures of Wadsworth & Dybwad (1998). The emissivity values corresponding to central wavelength of fluke camera (10–11 μm) were used to estimate the calibrated day and night temperatures.

The albedo and temperature data measured in the field with GPS coordinates were subsequently plotted against the albedo and temperature of satellite data at respective locations. It is evident from Figs 3(A) and (B) that the field and satellite data correlate very well and the relationship is statistically significant ($R^2 = 0.78$ to 0.89) at 95 per cent. This empirical relationship is used to generate calibrated, diurnal, satellite datasets. Since emissivity of dry rocks and dry soils does not change, the adopted procedure is expected to yield meaningful transformations.

4.1.2 Geometric correction, estimation of albedo and temperature difference

Since thermal inertia computation involves visible and thermal infrared bands of varying spatial resolutions, spatial re-sampling and accurate co-registration of datasets are necessary. The GPS data collected in the field for prominent roads and road–river intersections (at 20 locations) were used to geometrically correct the daytime visible bands with 15 m spatial resolution using ERDAS imaging software. Subsequently, both visible and thermal bands were re-sampled to 30 m spatial resolution and co-registered. Similarly, nighttime data were also re-sampled to 30 m and co-registered with daytime data. Root mean square error (RMSE) ranged between 0.006 and 0.009 m with a maximum positional error up to 27 cm on the ground.

Since albedo offers important information on the absorbed energy, broad band albedo needs to be estimated from the reflective bands of daytime ASTER data. In this study, we have estimated the total broadband albedo (β_T) using eq. 9 proposed by Liang *et al.* (2006). For this purpose, the surface reflectances (AST07) of band 1 to band 9 were used. Since the investigated area is a flat terrain, no topography-related corrections are necessary.

$$\beta_T = 0.82\beta_1 + 0.183\beta_2 - 0.034\beta_3 - 0.085\beta_4 - 0.298\beta_5 + 0.356\beta_6 + 0.239\beta_7 - 0.24\beta_9 - 0.0001. \quad (9)$$

The daytime and nighttime temperature difference image (ΔT) was generated by subtracting the recalibrated daytime and nighttime images using the ERDAS modeller.

4.2 Thermal inertia estimation

4.2.1 LUT approach

In this study, we used a thermal model to generate a LUT relating temperature difference (ΔT), thermal inertia and albedo following the procedures of Pratt & Ellyett (1979) and Mitra & Majumdar (2004). The LUT (Fig. 4) was generated by considering flat topography, low wind velocity (3.5 m s^{-1}), minimum and maximum air temperature of 15 and 30 °C and radiative sky temperature of −20 °C.

Table 2. Thermal conductivity of investigated rocks *vis-à-vis* published results.

Rock types	Thermal diffusivity $\times 10^{-6}$ m^2 s^{-1}		Thermal conductivity (J m^{-1} K^{-1} s^{-1})	
	Value measured	Published	Value measured	Published
Granite	1.02	0.93–1.787[c]	1.71	1.5–2.5[a]
Charnockite	0.87	1.25–1.85 [b]	1.72	2.13–2.81[b]
Garnet gneiss	0.83	1.15[b]	2.00	2.20[a]
Basic granulite	0.80	1.17–1.29[b]	2.20	2.27–2.6[b]
BMQ	1.49	DNA	2.68	DNA
Metabasite	0.68	DNA	1.65	1.84[c], 2.20[a]
Norite	0.80	DNA	1.91	1.7–2.5, 2.10–2.30[a]
Migmatite	1.02	DNA	1.89	1.8–2.4[b]
Migmatite with mineralization	1.16	DNA	2.09	DNA

[a]Cote & Cornrad (2005), [b]Ray *et al.* (2006), [c]Horai & Baldridge (1971), [d]Kim *et al.* (2007), DNA—Data not available.

Table 3. Comparison of thermal inertia of different rocks at coarse, medium and fine resolutions.

	Field measured				ASTER derived						Laboratory Measured
	Albedo (β)	ΔT (°C)	TI_{ATIM} (J m^{-2} K^{-1} s$^{-1/2}$)	TI_{LUT} J m^{-2} K^{-1} s$^{-1/2}$)	Albedo (β)		ΔT (°C)		TI_{ATIM} (J m^{-2} K^{-1} s$^{-1/2}$)		TI_{LUT} (J m^{-2} K^{-1} s$^{-1/2}$)		TI_{Lab} (J m^{-2} K^{-1} s$^{-1/2}$)
					Min	Max	Min	Max	Min	Max	Min	Max	
Charnockite	0.09	10	9839	7522	0.05	0.09	11.7	13.7	7478	9065	5407	7547	1825
Basic granulite	0.14	14	3476	2364	0.08	0.11	12.2	14.8	6140	7871	4433	6089	1958
Dolerite dyke	0.11	15	6029	4442	0.08	0.12	14.5	16.8	5666	6757	3987	4581	2014
Migmatite	0.14	11	7917	6234	0.07	0.13	14.3	15.4	5935	6652	4429	4935	1825
Migmatite + mineralization	0.43	15	5474	3889	0.1	0.15	15.2	15.9	5698	6447	4037	4864	1764
BMQ	0.06	25	3857	2023	0.09	0.12	14.9	16.5	5523	5901	4005	4517	1958
Gossan/laterite soils	0.09	24	3874	2118	0.14	0.32	15.9	16.9	5407	5753	3697	3783	1796
Water body			N.M.		0.09	0.11	9.8	12.8	7164	9474	5959	7482	N.M.
Soil over migmatite	0.18	10	7969	6615	0.11	0.14	12.2	15.3	5831	6260	4088	4552	1927
Soil over charnockite			N.M.		0.08	0.12	12.1	14.5	6497	7316	4943	5583	2272

N.M. = Not measured.

For each pixel of the image, thermal inertia was then estimated using the derived predictive equations in Matlab.

4.2.2 ATIM approach

For this approach, the variables were collected from the local meteorological station (t_{max}, C_t), and satellite scenes (β, ΔT, t_1, t_2) and established values from the literature (Xue & Cracknell 1993, 1995). The value of parameters used in above eqs (3)–(8) include S_0 (1.361 kw m^{-2}), C_t (0.75), ω (7.27×10^{-5} rad s^{-1}), t_{max} (32 400 s), δ (−9.53°) and ϑ (11.989161). For each satellite image pixels, thermal inertia was calculated using Matlab.

4.3 Laboratory measurements

Rock and soil samples collected from the field representing the ore body, alteration zones and country rock were analysed for mineralogy and thermal properties. For mineral identification, petrography was used. Thermal properties like conductivity, diffusivity and inertia were estimated using a self-fabricated, cost-effective apparatus (Ramakrishnan *et al.* 2012) which can be used under steady-state and transient techniques.

Mineralogy and major oxide chemistry of samples collected from field were estimated by conventional procedures such as petrography, X-ray diffractometry (XRD) and fluorescence (XRF). The XRF instrument (PW-2404) was calibrated using the USGS standards Sco-1, SGR-1 and Sdo-1 (Govindaraju 1994).The weight percentage of major oxides was used to identify lithology and ore minerals in conjunction with petrography results.

5 RESULTS

5.1 Mineralogy of ore bodies, alteration zones and host rocks

From ore petrography studies (Figs 5A–D), it is clear that pyrite (Py), chalcopyrite (Chpy), galena (Gl) and sphalerite (Sph) are the main sulphide minerals in this prospect. In addition to these, a few grains of malachite, marcasite, azurite, gold, bornite, pyrrhotite and molybdenite are also evidenced under microscope. Though the abovementioned major minerals (Chpy, Gl and Sph) are found in varying amounts, two dominant mineral associations can be distinctly observed. This includes a zone of sphalerite–galena–chalcopyrite in northern zone (samples S4, S6 and S9) and a zone of chalcopyrite and pyrite (samples A5 and A83) in southern zone of mineralization. Chalcopyrite and sphalerite are found as medium to coarse-grained crystals with intergranular and cataclastic texture with pyrite and pyrrhotite (Fig. 5B). Based on geochemistry, this prospect is predominantly rich in Zn (2.2–14 per cent) with subordinate amount of Cu (0.16–1.0 per cent) and Pb (0.17–1.86 per cent). The alteration of host rock is mainly manifested by development of thin biotite, chlorite zones, alteration of feldspar into kaolinite and pyroxenes into actinoloite and tremolite (A5 and Z2). At many places (A11, A41 and A7), the effect of secondary enrichment is evidenced by the prevalence of gossans.

In case of country rocks, mafic granulites (Fig. 5E) contain about 55–60 per cent of Fe–Mg minerals (such as hypersthene [Hp], hornblende [Hb], biotite [Bt] and cordierite [Cd]), 35–40 per cent of albite [Plg] and quartz [Qz]. The charnockite (Fig. 5F) contains quartz (25–30 per cent), albite (8–10 per cent), orthoclase [Ortho]

(5–8 per cent), hyperesthene (15–20 per cent) and cordierite (25–30 per cent). The dolerite dykes (Fig. 5G) contain hypersthene (15–20 per cent) in addition to other essential minerals such as labradorite, olivine [Olv] and augite [Aug]. The migmatite and granite gneiss (Fig. 5H) have predominance of quartz (30–40 per cent) and potash feldspar (15–25 per cent) with subordinate amounts of albite, hornblende and garnet.

5.2 *In situ* thermal properties

The thermal diffusivity and conductivity estimated in laboratory is presented in Table 2. At room temperature, thermal conductivity of SiO_2-rich rocks (67–74 per cent) ranges from 1.6 to 1.9 J m^{-1} s^{-1} K^{-1}, whereas conductivity of mafic (MgO and FeO) rocks is from 1.7 to 2.2 J m^{-1} s^{-1} K^{-1}. The mineralized areas, gossans, banded magnetite quartzite and migmatites with high magnetite content are observed to show higher conductivity values (2.09–2.19 J m^{-1} s^{-1} K^{-1}) than their non-mineralized counter parts (1.5–1.9 J m^{-1} s^{-1} K^{-1}). The experiments were repeated to check the consistency and it was observed that both transient and steady-state methods yielded highly reproducible results within an error limit of ±0.3 J m^{-1} s^{-1} K^{-1}. This error range is less than the values (0.2 ± 0.1–3.4 ± 3.0 J m^{-1} s^{-1} K^{-1}) published in literature for various rocks (Beardsmore & Cull 2001).

5.3 Thermal inertia mapping

It is clear from the above results that mineralogy plays a vital role in heat transfer and affects thermal conductivity, diffusivity and inertia. Hence, changes in surface temperature of rocks and soils mainly

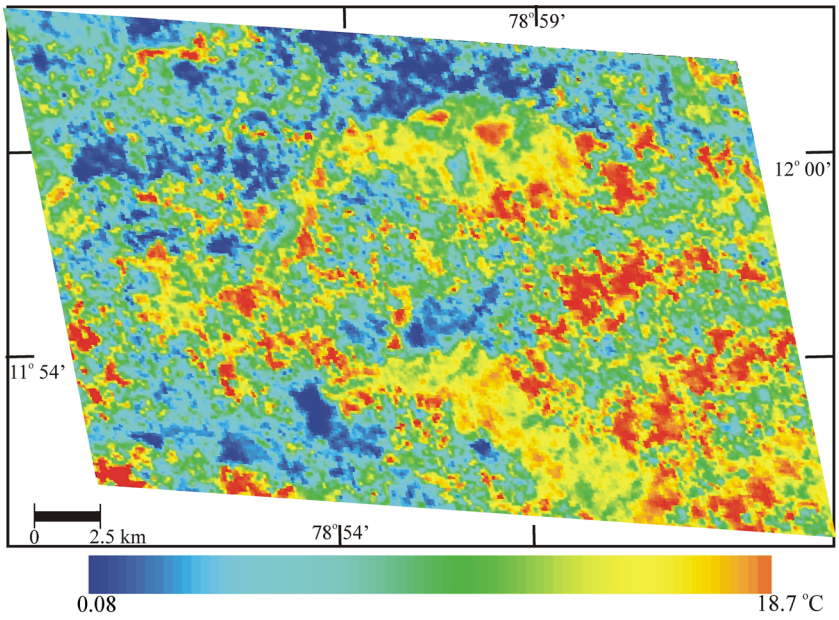

Figure 6. Map showing the temperature difference (ΔT) between daytime and nighttime images.

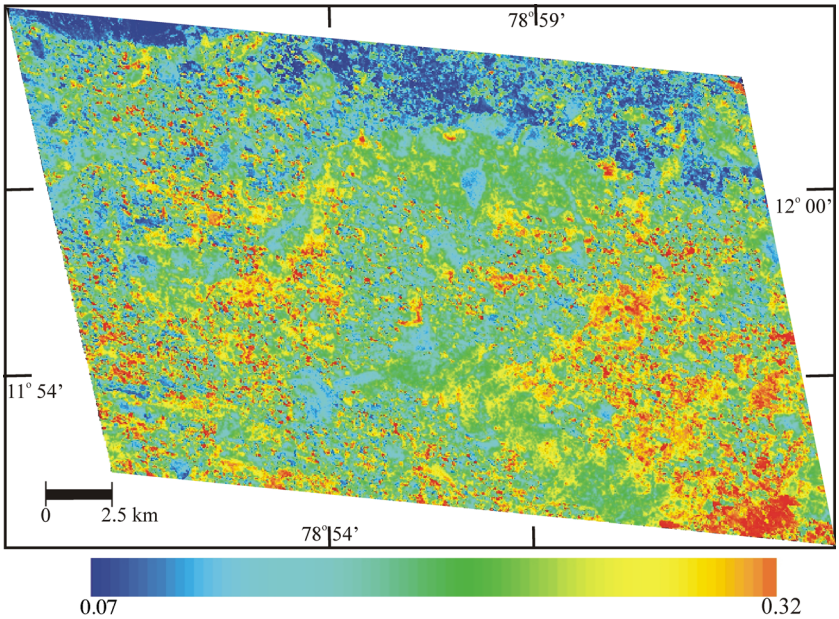

Figure 7. Map depicting the variations in albedo from different rock and soil types.

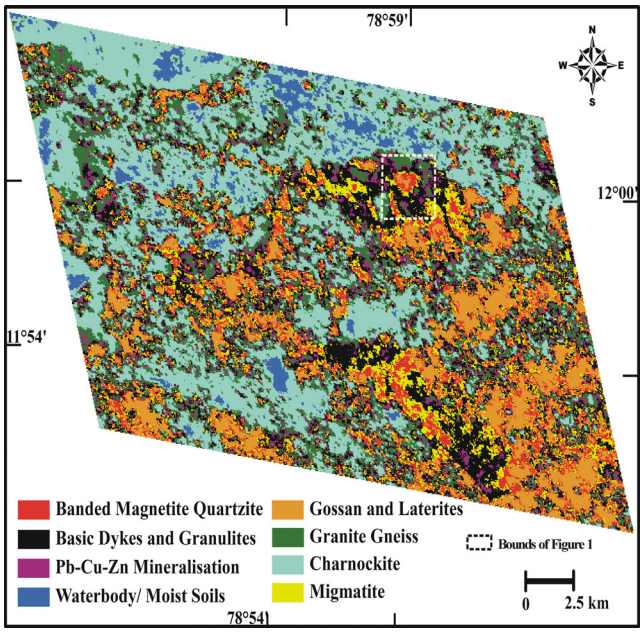

Figure 8. Thermal inertia map estimated by LUT method.

depend on its thermal inertia characteristics. In a diurnal heating and cooling cycle, changes in thermal inertia of the Earth surface materials manifest in terms of thermal contrast (ΔT). In this study, we estimated ΔT (temperature difference between the daytime and nighttime) using ASTER data sets. It is evident from Table 3 and Fig. 6 that the thermal contrast was the least, as expected, in water bodies and water logged areas. Among different rock exposures, charnockite has the lowest thermal contrast (11.7–13.7 °C). The maximum contrast is observed in the metallic ore bearing rocks like gossan, laterite, BMQ and migmatite with polymetal mineralization (14.9–16.9 °C). The basic rocks (dolerite dykes and basic granulites) have slightly higher temperature difference (12.2–16.8 °C) than the acidic rocks like granite gneiss and migmatite (14.0–15.5 °C).

Broadband albedo (Fig. 7), a measure of energy reflected by a given surface, indicates that gossans and laterites exhibit maximum albedo (0.32). The basic rocks and charnockites have the least albedo (0.05–0.12) and the acidic rocks (migmatite and granite gneiss) and the regolith developed over it have moderate albedo (0.7–0.15).

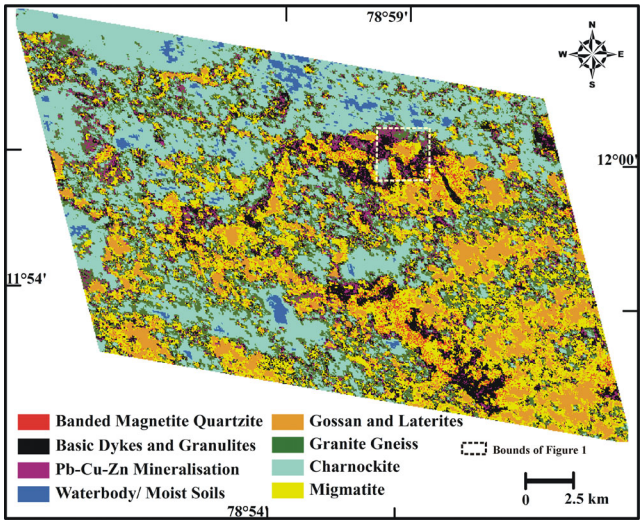

Figure 9. Thermal inertia map derived by ATIM method.

Using the ASTER temperature difference and albedo images, thermal inertia maps were generated by LUT (Fig. 8) and ATIM (Fig. 9) approaches. It is evident from Table 3 and Figs 8 and 9 that water bodies and water logged areas show the highest thermal inertia (TI_{LUT} = 5959–7482 J m^{-2} K^{-1} s$^{-1/2}$, TI_{ATIM} = 7164–9474 J m^{-2} K^{-1} s$^{-1/2}$) and the mineralized areas show the least resistance for heat transfer/dissipation (TI_{LUT} = 3697–4864 J m^{-2} K^{-1} s$^{-1/2}$, TI_{ATIM} = 5407–6447 J m^{-2} K^{-1} s$^{-1/2}$). This observation is in agreement with the thermal properties of water and ore minerals. Among different rocks, the charnockite is observed to show maximum thermal inertia by both methods (TI_{LUT} = 5407–7547 J m^{-2} K^{-1} s$^{-1/2}$, TI_{ATIM} = 7478–9065 J m^{-2} K^{-1} s$^{-1/2}$). Whereas gossans, BMQ and migmatite with Pb–Cu–Zn mineralization have low thermal inertia. Similarly, the acidic rocks (migmatite and gneisses) could be discriminated from basic granulite and dolerite dyke based on the range of thermal inertia values. Such discrimination of mineralized areas and litho types based on thermal inertia is also possible at field scales. The thermal inertia ranges estimated using the FLUKE thermal images (Table 3) also indicate the lowest values corresponding to mineralized areas (TI_{LUT} = 2118–3889 J m^{-2} K^{-1} s$^{-1/2}$, TI_{ATIM} = 3874–5474 J m^{-2} K^{-1} s$^{-1/2}$). Akin to the satellite-derived results, different acidic and basic litho types can also be discriminated from the field measurements.

Scatter plot relating the thermal inertia estimated by both LUT and ATIM methods matches very well (R^2 = 0.89–0.97) at both satellite (Fig. 10) and field scales (Fig. 11A) with 95 per cent statistical significance. Therefore, results arrived by both techniques are consistent, meaningful and can be used to discriminate the mineralized areas and various rock types. In addition, it is interesting to note that the thermal inertia derived from satellite data correlate reasonably well (R^2 = 0.69–0.72) with field observation for various litho types and mineralized areas (Figs 11B and C) at 80 per cent significance levels. However, the laboratory-measured values matched neither with satellite data nor with the field data.

To evaluate classwise accuracy, a confusion matrix was (Table 4) calculated involving 124 pixels and associated ground truth data. User's and producer's classification accuracy for the mineralized areas (zones of principal interest) is 80.9 per cent. For other rocks, the user's accuracy varied from 43.7 to 86.2 per cent. The lowest user's accuracy was observed in basic dykes (43.7 per cent). Table 4 indicates that 25 per cent of pixels representing basic dykes are misclassified as charnockites. This is attributed to prevalence of basic and intermediate charnockites in the investigated area, the composition of which is similar to basic dykes. The producer's accuracy for all classes is relatively satisfactory and ranges from 61.5 to 91.6 per cent.

6 DISCUSSIONS

Over the last two decades, remote thermal inertia mapping has been gaining importance in geology and planetary-exploration-related applications (Kahle *et al.* 1976; Kahle 1977; Pratt & Ellyett 1979; Jakosky *et al.* 2000; Arvidson *et al.* 2003; Majumdar 2003; Mitra & Majumdar 2004; Eneva *et al.* 2006; Fergason *et al.* 2006; Nowicki & Christensen 2007; Putzig & Mellon 2007; Brenning *et al.* 2011; Piqueux & Christensen 2011). However, most of the above works have minimum or no field inputs to validate correctness of the satellite-derived results. From this perspective, this study attains significance, as we attempted to compare the remotely

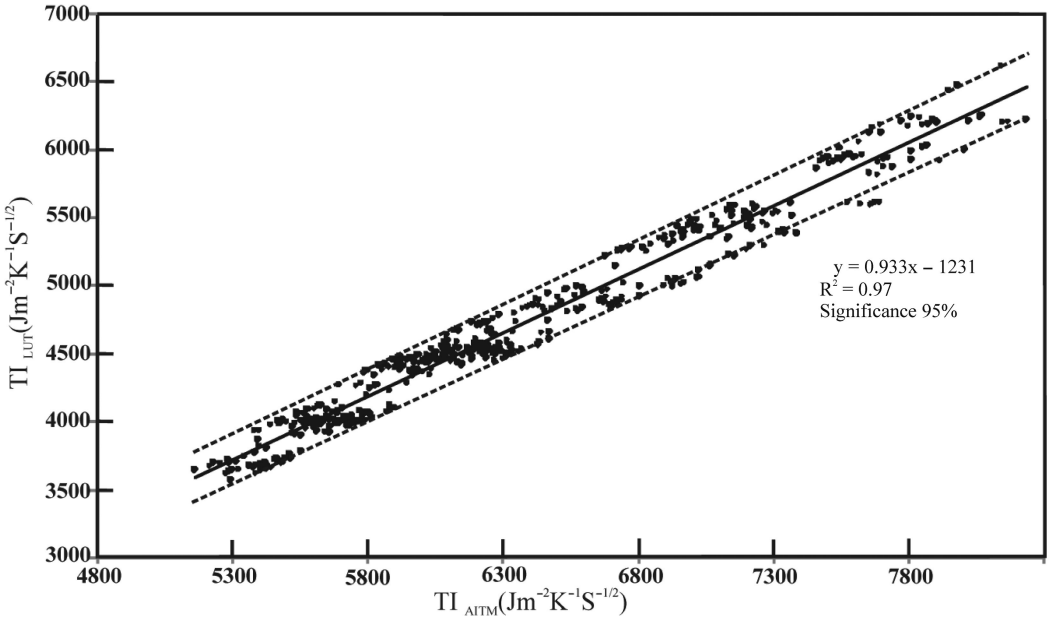

Figure 10. Scatter plot depicting the linear relationship between thermal inertias estimated by LUT and ATIM methods and ASTER data.

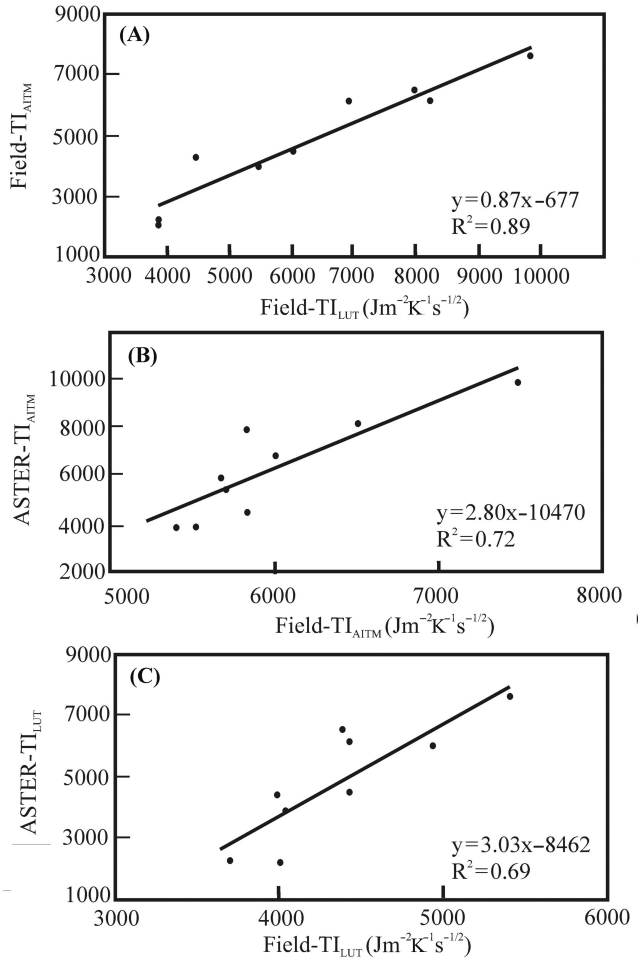

Figure 11. (A) Scatter plots showing the relationship between the thermal inertia measured by LUT and ATIM in the field. Interrelation between satellite and field measurements (by LUT and ATIM) is shown in (B) and (C), respectively.

derived thermal properties with field- and laboratory-measured values. Further, we have also carried out detailed compositional and petro-physical analysis of samples (representing ore mineralization, rock- and soil-type changes) and related them to changes in thermal inertia.

Thermal properties of metamorphic rocks and associated soils are poorly understood because of limited data on basic thermal properties (conductivity and diffusivity) and influencing properties (mineralogy, chemistry, bulk density, grain size and moisture content). For rocks and soils, thermal properties are often estimated by assuming that the heat transfer mechanism is conduction (Sass *et al.* 1971). However, convection and radiative heat transfer can adversely affect the estimates of bulk thermal properties of the rocks (Clauser & Huenges 1995; Gehlin & Hellström 2003). These observations suggest that the conductivity estimated in the laboratory conditions has limited utility in applications involving the thermal properties of *in-situ* exposures of rocks and soils (Sass *et al.* 1971). In this study, we attempted to estimate thermal properties of rocks and soils at three different scales, namely coarse (30 m^2), moderate (1.5 m^2) and fine (0.09 m^2) scales using satellite data, field thermal imager and a self-fabricated laboratory setup.

It is evident from Table 2 that the samples representing ore minerals (BMQ, gossan and poly metals) have higher thermal conductivity than the host rocks. Similarly, the thermal conductivity of granite and migmatite (acid rocks) is lower than basic rocks such as norite, basic granulite and dolerite. These observations are comparable to the results published in literature (Horai & Baldridge 1972; Cote & Cornard 2005; Ray *et al.* 2006; Kim *et al.* 2007).

For field-based measurements of thermal inertia, we used a thermal imager to acquire the albedo and temperature images of rock and soil exposures ranging in size from 1.0 to 1.5 m^2. For each litho type, we used the median values of albedo and ΔT to calculate the thermal inertia by LUT and ATIM methods (Table 3). It is observed that the exposures with ore mineralization have maximum thermal contrast and low thermal inertia. Whereas country rocks without ore minerals have lower thermal contrast and moderate inertia. It is also evident from the results that it is possible to discriminate the litho types based on thermal inertia. Typically, charnockite and

Table 4. Confusion matrix depicting the classification accuracy.

	Ground information									
Thermal inertia map	Basic dyke	BMQ	Charnockite	Gossan &	Granite	Migmatite	Mineralization	Water body	No. of classified pixels	User's accuracy
Basic dyke	7	1	4	1	1	0	2	0	16	43.7 per cent
BMQ	0	8	0	0	0	0	2	0	10	80.0 per cent
Charnockite	1	0	25	1	1	0	0	1	29	86.2 per cent
Gossan & Laterites	0	0	1	12	1	0	0	0	14	85.7 per cent
Granite gneiss	0	0	1	1	8	1	0	0	11	72.7 per cent
Migmatite	0	0	2	1	0	9	0	0	12	75 per cent
Mineralization	0	0	0	1	2	1	17	0	21	80.9 per cent
Water body	0	0	0	0	0	0	0	11	11	100.0 per cent
No. of ground truth pixels	8	9	33	17	13	11	21	12	124 Total no. of pixels used for accuracy assessment	
Producer's accuracy	87.5 per cent	88.8 per cent	75.7 per cent	70.5 per cent	61.5 per cent	81.8 per cent	80.9 per cent	91.6 per cent		

$$\text{Overall accuracy} = \frac{\text{Total no. of correct classified pixel}}{\text{Total no. of pixel used for classification}} = 78.2 \text{ per cent, Kappa } (k) = 0.725.$$

basic rocks are found to have high inertia (TI_{ATIM} = 9838–6029 J m^{-2} K^{-1} $s^{-1/2}$, TI_{LUT} = 7521–4442 J m^{-2} K^{-1} $s^{-1/2}$); granite gneiss and migmatite have moderate inertia (TI_{ATIM} = 6919–5474 J m^{-2} K^{-1} $s^{-1/2}$, TI_{LUT} = 5234–3889 J m^{-2} K^{-1} $s^{-1/2}$); and BMQ, gossan, laterite and polymetal mineralized areas have low thermal inertia (TI_{ATIM} = 3874–5474 J m^{-2} K^{-1} $s^{-1/2}$, TI_{LUT} = 2118–3889 J m^{-2} K^{-1} $s^{-1/2}$).

The satellite-data-derived thermal inertial values (Figs 8 and 9) also show similar trend (Table 3) enabling delineation of mineralized zones and lithological variations over a large area. In this study, we used a new procedure to transform the multidate daytime and nighttime ASTER images to a common reference frame with the aid of field-measured temperature and albedo data. Though normalization of satellite data with field data can introduce some inaccuracies in LUT, it is observed to generate practically meaningful thermal inertia map. The derived thermal inertia maps correlate mutually and with field-measured values (Table 3 and 4; Figs 10 and 11). Further, existence of good correlation between LUT and ATIM (at field- and image-scale) techniques (R^2 = 0.96 at 95 per cent significance levels) can be interpreted that the normalization did not affect the results estimated by LUT significantly. Poor correlation between laboratory- and satellite-measured TI values is attributed to heterogeneity and variations in bulk properties at field and satellite scales.

Since the ore bodies have high thermal conductivity, the thermal inertia of the mineralized (Fe, Pb, Cu and Zn) areas has very high ΔT and very low inertia. In relating the thermal properties of rocks as a function of constituent mineralogy, Höfer & Schilling (2002) elucidated that thermal diffusivity is greatly influenced by amount of quartz, which has the highest thermal diffusivity among the major minerals. Pyroxene, amphibole and garnet display intermediate diffusivities, and feldspars are of minor importance owing to their low diffusivity. Since basic rocks and pyroxene granulites (charnockite) do not have any free quartz, they are observed to show high thermal inertia. For the same area, Ramakrishnan *et al.* (2012) reported that both thermal conductivity and diffusivity are sensitive to $SiO_2/(MgO+Fe_2O_3)$ ratio. This ratio is often used to discriminate the felsic and mafic granulites (Miyashiro 1974). The felsic rocks such as granite and migmatite with high percentage of quartz have a higher diffusivity values (10.8–11.5 × 10^{-7} m^2 s^{-1}) than the mafic rocks dominated by pyroxenes, olivine and feldspar (7.74–9.95 × 10^{-7} m^2 s^{-1}). This indicates that in the case of basic rocks, where no free quartz exists, the specific heat capacity of Fe–Mg minerals plays a critical role in thermal diffusivity. Höfer & Schilling (2002) and Ray *et al.* (2006) also reported similar observations. For soils, it is evident that with increase in fines content, both conductivity and diffusivity reduce. This observation is akin to the results reported by Abu-Hamdeh (2003), wherein increase in clay content was attributed to increase in volumetric-specific heat. In this study, thermal properties of soils are found to be consistent with that of parent rocks.

Since ASTER thermal bands have coarse spatial resolution (90 m), the best possible mapping scale is about 1:100 000. Accordingly, the lithologies demarcated in this study can serve as a regional geological map. Nevertheless, the mineralization areas are very prominent even at this scale due to sharp contrast in thermal conductivity values.

7 CONCLUSIONS

Following conclusions emerge from this study:

1. The procedure adopted herein is capable of distinguishing mineralized areas from host rocks due to their low thermal inertia. The petrography and SEM studies reveal that the regions delineated for low thermal inertia host Pb–Cu–Zn deposit and BMQ. Hence, the adopted procedure can be employed in exploring the exposed and shallow-buried ore bodies.

2. Among the country rocks, charnockite and basic rocks have high thermal inertia than the migmatite and granite gneiss. This mineralogy-influenced change in thermal conductivity (Ramakrishnan *et al.* 2012) can be used to discriminate and map the rock types. Overall accuracy of classification is 78 per cent.

3. The thermal inertia estimated by LUT and ATIM methods correlate well and has the potential to discern the rock types and mineralized areas. However, they need to be considered as apparent thermal inertia values as they do not commensurate with laboratory-measured values.

ACKNOWLEDGEMENTS

Authors acknowledge the Department of Science and Technology, Government of India for supporting this research (Grant no: NRDMS/11/1291/2007). D.R. acknowledges Prof. Dr. J. H. Schön and an anonymous reviewer for critical evaluation and constructive comments that were very useful in improving the quality of the paper.

REFERENCES

Abu-Hamdeh, N.H., 2003. Thermal properties of soils affected by density and water content, *Bio-syst. Eng.,* **86**(1), 97–102.

Arvidson, R.E. *et al.*, 2003. Mantled and exhumed terrains in Terra Meridiani, Mars, *J. geophys. Res.,* **108**(E12), 8073.

ASTM, 2008. Standard test method for determination of thermal conductivity of soil and soft rock by thermal needle probe procedure, *ASTM Data Ser. Publ.,* **D5334-08,** 1–8.

ASTM, 2009a. Standard practice for thermal diffusivity by the flash method, *ASTM Data Ser. Publ.,* **E2585-09,** 1–10.

ASTM, 2009b. Standard test method for thermal conductivity of refractories, *ASTM Data Ser. Publ.,* **C201-93,** 1–6.

Bautista, M.O. & Campos, F.I., 2005. Transient heat conduction in a solid slab using multiple-scale analysis, *Heat Trans. Res.,* **42,** 150–157.

Beardsmore, G.R. & Cull, J.P., 2001. *Crustal Flow: A Guide to Measurement and Modeling,* Cambridge University Press, 324 pp.

Beck, A.E., 1976. An improved method of computing the thermal conductivity of fluid-filled sedimentary rocks, *Geophysics,* **41,** 133–144.

Bosch, M., Zamora, M. & Utama, W., 2002. Lithology discrimination from physical rock properties, *Geophysics,* **67,** 573–581.

Brenning, A., Peña, M.A., Long & Soliman, A., 2011. Thermal remote sensing of ice-debris landforms using ASTER, *The Cryosphere Discuss,* **5,** 2895–2933.

Cai, G., Du, M., Xue, Y. & Li, S., 2008. Analysis of an urban heat sink using thermal inertia model from ASTER data in Beijing, China, in *Proceedings of IGARSS,* pp. 1346–1349.

Carslaw, H.S. & Jaeger, J.C., 1959. *Conduction of Heat in Solids,* Oxford University Press Inc., p. 510.

Chattopadhyay, P.K., 1999. Zn-spinel in the metamorphosed Zn-Pb-Cu sulphide deposit at Mamandur, Southern India, *Mineral. Mag.,* **63**(5), 743–755.

Christensen, P.R. & Malin, M.C., 1988. High resolution thermal imaging of Mars, *Lunar planet. Sci.,* **XIX,** 180–181.

Clauser, C. & Huenges, E., 1995. Thermal conductivity of rocks and minerals. Rock physics and phase relations: a handbook of physical constants, *AGU Ref. Shelf*, **3**, 105–125.

Coolbaugh, M.F., Kratt, C., Fallacaro, A., Calvin, W.M. & Taranik, J.V., 2007. Detection of geothermal anomalies using Advanced Spaceborne Thermal Emission and Reflection Radiometer (ASTER) thermal infrared images at Bradys Hot Springs, Nevada, USA, *Remote Sens. Environ.,* **106,** 350–359.

Cote, J. & Cornard, J.M., 2005. A generalized thermal conductivity model for soils and construction materials, *Can. Geotech. J.,* **42**(2), 443–458.

Deans, J., Gerhard, J. & Carter, L.J., 2006. Analysis of a thermal imaging method for landmine detection, using infrared heating of the sand surface, *Infrared Phys. Technol.,* **48,** 208–216.

El Sayed, A.M.A., 2011. Thermophysical study of sandstone reservoir rocks, *J. Petrol. Sci. Eng.,* **76,** 138–147.

Eneva, M., Coolbaugh, M. & Combs, J., 2006. Application of satellite thermal Infrared imagery to geothermal exploration in East Central California, *GRC Trans.,* **30,** 407–411.

Facer, R.A., Cook, A.C. & Beck, A.E., 1980. Thermal properties of coal rank in ranks and coal seams of the southern Sydney basin, New South Wales—a palaeogeothermal explanation of coalification, *Int. J. Coal Geol.,* **1,** 1–17.

Fergason, R.L., Christensen, P.R. & Kieffer, H.H., 2006. High-resolution thermal inertia derived from the thermal emission imaging system (THEMIS): thermal model and applications, *J. geophys. Res.,* **111,** E12004.

Gehlin, S.E.A. & Hellström, G., 2003. Influence on thermal response test by groundwater flow in vertical fractures in hard rock, *Renewable Energy,* **28**(14), 2221–2238.

Gillespie, A.R. & Kahle, A.B., 1977. Construction and interpretation of a digital thermal inertia image, *Photogramm. Eng. Remote Sens.,* **43,** 983–1000.

Govindaraju, K., 1994. Compilations of working values and sample description for 383 geostandards, *Geo-stand. News Lett.,* **18,** 1–158.

Gupta, R.P., Chakraborty, R. & Awasthi, A.K., 2009. Satellite data can cost effectively show oil field thermal anomalies, *Oil Gas J.,* **107**(41), 34–36.

Hofer, M. & Schilling, F.R., 2002. Heat transfer in quartz, orthoclase and sanidine at elevated temperature, *Phys. Chem. Miner.,* **29,** 571–584.

Horai, K. & Baldridge, S., 1972. Thermal conductivity of nineteen igneous rocks, *Phys. Earth planet. Inter.,* **5,** 151–166.

Jakosky, B.M., Mellon, M.T., Kieffer, H.H., Christensen, P.R., Varnes, E.S. & Lee, S.W., 2000. The thermal inertia of Mars from the Mars global surveyor thermal emission spectrometer, *J. geophys. Res.,* **105,** 9643–965.

Jougnot, D. & Revil, A., 2010. Thermal conductivity of unsaturated clay-rocks, *Hydrol. Earth Syst. Sci.,* **14,** 91–98.

Kahle, A.B., 1977. A simple thermal model of the Earth's surface for geologic mapping by remote sensing, *J. geophys. Res.,* **82,** 1673–1680.

Kahle, A.B., 1987. Surface emittance, temperature, and thermal inertia derived from thermal infrared multispectral scanner (TIMS) data for Death Valley, California, *Geophysics,* **52**(7), 858–874.

Kahle, A.B., Gillespie, A.R. & Goetz, A.F.H., 1976. Thermal inertia imaging: a new geologic mapping tool, *Geophys. Res. Lett.,* **3**(1), 26–28.

Kim, J., Lee, Y. & Koo, M., 2007. Thermal properties of granites from Korea, American Geophysical Union, Fall Meeting, #T11B-0576.

Liang, S., Zheng, T., Liu, R., Fang, H., Tsay, S.C. & Running, S., 2006. Estimation of incident photosynthetically active radiation from MODIS data, *J. geophys. Res. Atmosphere,* **111,** D15208.

Lu, S., Ju, Z., Ren, T. & Horton, R., 2009. A general approach to estimate soil water content from thermal inertia, *Agric. Forest Meteorol.,* **149,** 1693–1698.

Majumdar, T.J., 2003. Regional thermal inertia mapping over the Indian subcontinent using INSAT-1D VHRR data and its possible geological applications, *Int. J. Remote Sens.,* **24,** 2207–2220.

Mellon, M.T., Jakosky, B.M. & Kieffer, H.H., 2000. High resolution thermal inertia mapping from the Mars global surveyor thermal emission spectrometer, *Icarus,* **148,** 437–455.

Middleton, M.F., 1993. A transient method of measuring the thermal properties of rocks, *Geophysics,* **58,** 357–365.

Minacapilli, M., Iovino, M. & Blanda, F., 2009. High resolution remote estimation of soil surface water content by a thermal inertia approach, *J. Hydrol.,* **379,** 229–238.

Mitra, D.S. & Majumdar, T.J., 2004. Thermal inertia mapping over the Brahmaputra basin, India using NOAA AVHRR data and its possible geological applications, *Int. J. Remote Sens.,* **25,** 3245–3260.

Miyashiro, A., 1974. Volcanic rock series in island arcs and active continental margins, *Am. J. Sci.,* **274,** 321–355.

Morabito, P., 1989. Thermal conductivity and diffusivity measurements by the transient two linear and parallel probe method, *Thermochim. Acta,* **148,** 513–520.

Mwenifumbo, C.J., 1993. Temperature logging in mineral exploration, *J. appl. Geophys.,* **30,** 297–313.

Nash, D.B., 1988. Detection of a buried horizon with a high thermal diffusivity using thermal remote sensing, *Photogramm. Eng. Remote Sens.,* **54,** 1437–1446.

Nasipuri, P., Majumdar, T.J. & Mitra, D.S., 2006. Study of high-resolution thermal inertia over western India oil fields using ASTER data, *Acta Astronautica,* **58,** 270–278.

Nowicki, S.A. & Christensen, P.R., 2007. Rock abundance on mars from the thermal emission spectrometer, *J. geophys. Res.,* **112,** E05007.

Piqueux, S. & Christensen, P.R., 2011. Temperature dependent thermal inertia of homogeneous Martian regolith, *J. geophys. Res.,* **116,** E07004.

Pratt, D.A. & Ellyett, C.D., 1979. The thermal inertia approach to mapping soil moisture and geology, *Remote Sens. Environ.,* **8,** 151–158.

Prensky, S., 1992. Temperature measurements in boreholes: an overview of engineering and scientific applications, *Log Anal.,* **33**(3), 313–333.

Price, J.C., 1977. Thermal inertia mapping: a new view of the earth, *J. geophys. Res.,* **8,** 2582–2590.

Putzig, N.E. & Mellon, M.T., 2007. Apparent thermal inertia and the surface heterogeneity of Mars, *Icarus,* **191,** 68–94.

Putzig, N.E., Mellon, M.T., Jakosky, B.M., Pelkey, S.M., Martínez-Alonso, S., Hynek, B.M. & Murphy, N.W., 2004. Mars thermal inertia from Themis data, *Icarus,* **173,** 325–341.

Ramakrishnan, D., Bharti, R., Nithya, M., Kusuma, K.N. & Singh, K.D., 2012. Measurement of thermal properties of select intact and weathered granulites and their relationship to rock properties, *SEG Geophys.,* **77**(3), 63–73.

Ray, L., Forster, H.J., Schilling, F.R. & Forster, A., 2006. Thermal diffusivity of felsic to mafic granulites at elevated temperatures, *Earth planet. Sci. Lett.,* **251,** 241–253.

Sass, J.H., Lachenbruch, A.H. & Manroe, R.J., 1971. Thermal conductivity of rocks from measurements on fragments and its applications to heat flow determinations, *J. geophysics Res.,* **76,** 3391–3401.

Schieldge, J.P., Kahle, A.B., Alley, R.E. & Gillespie, A.R., 1980. Use of thermal inertia properties for material identification, *Image Process. Missile Guid., SPIE,* **238,** 350–357.

Schilling, F.R., 1999. A transient technique to measure thermal diffusivity at elevated temperatures, *Eur. J. Mineral.,* **11,** 1115–1124.

Schön, J.H., 2004. Physical properties of rocks: fundamentals and principles of petrophysics, in *Handbook of Geophysical Exploration Series,* Vol. 18, pp. 323–373, Elsevier.

Schön, J.H., 2011. Physical properties of rocks: a workbook, in *Handbook of Petroleum Exploration and Production,* Vol. 8, pp. 337–380, Elsevier.

Thompson, A.M. & Baker, R.N., 1981. Integrated geologic and remote sensing mineral exploration in Baja, California, in *Energy Resources on the Pacific region,* AAPG Special Volume (SG12), pp. 13–19.

Van Dam, R.L., Borchers, B., Hendrickx, J.M.H. & Hong, S.H., 2004. Controlled field experiments of wind effects on thermal signatures of buried and surface-laid land mines, in *Proceedings of International Society for Optical Engineering, SPIE,* Vol. 5415, pp. 648–657.

Vasseur, G., Brigaud, F. & Demongodin, L., 1995. Thermal conductivity estimation in sedimentary basins, *Tectonophysics,* **244,** 167–174.

Wadsworth, W. & Dybwad, J.P., 1998. A very fast imaging FT spectrometer for on line process monitoring and control, in *Proceedings of Electro-Optic, Integrated Optic, and Electronic Technologies for Online Chemical Process Monitoring, SPIE*, Vol. 3537, pp. 54–61.

Watson, K., 1971. Application of thermal modeling in the geological interpretation of IR images, in *Proceedings7th Int. Symp. Remote Sensing of Environment,* pp. 2017–2041.

Watson, K., 1973. Periodic heating of a layer over a semi-infinite solid, *J. geophys. Res.,* **78,** 5904–5910.

Watson, K., 1975. Geologic applications of thermal infrared images, *Proc. IEEE,* **63,** 128–137.

Woodside, W. & Messmer, J.H., 1961. Thermal conductivity of porous media (I. Unconsolidated porous sands, II. Consolidated rocks.), *J. appl. Phys.,* **32**(9), 1688–1699.

Xue, Y. & Cracknell, A.P., 1993. Advanced thermal inertia modeling and its application: modeling the emissivity of the ground, in *Proceeding of the 25th International Symposium on Remote Sensing and Global Environmental Change,* Graz, Austria, ERIM, Ann Arbor, II-121-II-122.

Xue, Y. & Cracknell, A.P., 1995. Advanced thermal inertia modeling, *Int. J. Remote Sens.,* **16,** 431–446.

Zolotarev, V.G., 1989. Thermal and energy factors of metal concentration in igneous plutons: an application to metallogenic analysis and exploration, *J. Geochem. Explor.,* **32,** 381–394.